Xtend, the Soft X-ray Imaging Telescope for the X-ray Imaging and Spectroscopy Mission (XRISM)

Koji Mori[a,b], Hiroshi Tomida[c], Hiroshi Nakajima[d,b], Takashi Okajima[e], Hirofumi Noda[f,g], Takaaki Tanaka[h], Hiroyuki Uchida[i], Kouichi Hagino[d], Shogo Benjamin Kobayashi[j], Hiromasa Suzuki[h], Tessei Yoshida[c], Hiroshi Murakami[k], Hideki Uchiyama[l], Masayoshi Nobukawa[m], Kumiko Nobukawa[n], Tomokage Yoneyama[b], Hironori Matsumoto[f,g], Takeshi Tsuru[i], Makoto Yamauchi[a], Isamu Hatsukade[a], Manabu Ishida[b], Yoshitomo Maeda[b], Takayuki Hayashi[e,o], Keisuke Tamura[e,o], Rozenn Boissay-Malaquin[e,o], Toshiki Sato[p], Junko Hiraga[q], Takayoshi Kohmura[r], Kazutaka Yamaoka[s], Tadayasu Dotani[b,t], Masanobu Ozaki[b], Hiroshi Tsunemi[f], Yoshiaki Kanemaru[a], Jin Sato[a], Toshiyuki Takaki[a], Yuta Terada[a], Keitaro Miyazaki[a], Kohei Kusunoki[a], Yoshinori Otsuka[a], Haruhiko Yokosu[a], Wakana Yonemaru[a], Yoh Asahina[d], Kazunori Asakura[f], Marina Yoshimoto[f], Yuichi Ode[f], Junya Sato[f], Tomohiro Hakamata[f], Mio Aoyagi[f], Yuma Aoki[n], Shun Tsunomachi[r], Toshiki Doi[r], Daiki Aoki[r], Kaito Fujisawa[r], Masatoshi Kitajima[r], and Kiyoshi Hayashida[f]

[a]Faculty of Engineering, University of Miyazaki, 1-1 Gakuen Kibanadai Nishi, Miyazaki, Miyazaki 889-2192, Japan

[b]Japan Aerospace Exploration Agency, Institute of Space and Astronautical Science, 3-1-1 Yoshino-dai, Chuo-ku, Sagamihara, Kanagawa 252-5210, Japan

[c]Japan Aerospace Exploration Agency, Institute of Space and Astronautical Science, 2-1-1, Sengen, Tsukuba, Ibaraki 305-8505, Japan

[d]College of Science and Engineering, Kanto Gakuinn University, Kanazawa-ku, Yokohama, Kanagawa 236-8501, Japan

[e]NASA's Goddard Space Flight Center, Greenbelt, MD 20771, USA

[f]Department of Earth and Space Science, Osaka University, 1-1 Machikaneyama-cho, Toyonaka, Osaka 560-0043, Japan

[g]Forefront Research Center, Osaka University, 1-1 Machikaneyama-cho, Toyonaka, Osaka 560-0043, Japan

[h]Department of Physics, Konan University, 8-9-1 Okamoto, Higashinada, Kobe, Hyogo 658-8501

[i]Department of Physics, Kyoto University, Kitashirakawa Oiwake-cho,Sakyo-ku, Kyoto, Kyoto 606-8502, Japan

[j]Department of Physics, Faculty of Science, Tokyo University of Science, Kagurazaka, Shinjuku-ku, Tokyo 162-0815, Japan

[k]Faculty of Liberal Arts, Tohoku Gakuin University, 2-1-1 Tenjinzawa, Izumi-ku, Sendai, Miyagi 981-3193, Japan

[l]Science Education, Faculty of Education, Shizuoka University, Suruga-ku, Shizuoka, Shizuoka 422-8529, Japan

[m]Faculty of Education, Nara University of Education, Nara, Nara 630-8528, Japan

[n]Department of Physics, Kindai University, 3-4-1 Kowakae, Higashi-Osaka, Osaka 577-8502, Japan

[o]Center for Space Science and Technology, University of Maryland, Baltimore County (UMBC), Baltimore, MD 21250, USA

arXiv:2303.07575v1 [astro-ph.IM] 14 Mar 2023

[p]Department of Physics, Rikkyo University, 3-34-1 Nishi Ikebukuro, Toshima-ku, Tokyo 171-8501, Japan
[q]Department of Physics, Kwansei Gakuin University, 2-2 Gakuen, Sanda, Hyogo 669-1337, Japan
[r]Department of Physics, Faculty of Science and Technology, Tokyo University of Science, 2641 Yamazaki, Noda, Chiba 270-8510, Japan
[s]Department of Physics, Nagoya University, Chikusa-ku, Nagoya, Aichi 464-8602, Japan
[t]Department of Space and Astronautical Science, School of Physical Sciences, SOKENDAI (The Graduate University for Advanced Studies), 3-1-1 Yoshino-dai, Chuou-Ku, Sagamihara, Kanagawa 252-5210, Japan

ABSTRACT

Xtend is a soft X-ray imaging telescope developed for the X-Ray Imaging and Spectroscopy Mission (XRISM). XRISM is scheduled to be launched in the Japanese fiscal year 2022. Xtend consists of the Soft X-ray Imager (SXI), an X-ray CCD camera, and the X-ray Mirror Assembly (XMA), a thin-foil-nested conically approximated Wolter-I optics. The SXI uses the P-channel, back-illuminated type CCD with an imaging area size of 31 mm on a side. The four CCD chips are arranged in a 2×2 grid and can be cooled down to −120 °C with a single-stage Stirling cooler. The XMA nests thin aluminum foils coated with gold in a confocal way with an outer diameter of 45 cm. A pre-collimator is installed in front of the X-ray mirror for the reduction of the stray light. Combining the SXI and XMA with a focal length of 5.6m, a field of view of $38' \times 38'$ over the energy range from 0.4 to 13 keV is realized. We have completed the fabrication of the flight model of both SXI and XMA. The performance verification has been successfully conducted in a series of sub-system level tests. We also carried out on-ground calibration measurements and the data analysis is ongoing.

Keywords: XRISM, Xtend, SXI, XMA, X-ray CCD, Back-illumination type CCD

1. INTRODUCTION

X-Ray Imaging and Spectroscopy Mission (XRISM) is the Japan's seventh X-ray astronomy mission and aimed at recovering one of the key scientific goals of the previous *Hitomi* mission, focusing only on the imaging and spectroscopy in the soft X-ray band.[1,2] XRISM is developed in the international collaboration of JAXA, NASA, ESA, and other institutes, and its launch is scheduled in the Japanese fiscal year 2022 on a JAXA H-IIA rocket. XRISM carries two telescopes, Xtend[3] and Resolve.[4] Xtend is a soft X-ray "imaging" telescope, while Resolve is a soft X-ray "spectroscopy" telescope. Each of them consists of an X-ray Mirror Assembly (XMA),[5] a thin-foil-nested conically approximated Wolter-I optics, and a focal plane detector with a focal length of 5.6 m. The focal plane detector of Xtend is the Soft X-ray Imager (SXI), an X-ray CCD camera,[6] while that of Resolve is an X-ray micro-calorimeter. Fig. 1 shows X-ray images of the Perseus Cluster and its central radio galaxy NGC 1275 taken with the *Hitomi* CCD camera and micro-calorimeter. Since the instrument design of XRISM are basically the same as those flown on *Hitomi*, this figure demonstrates the imaging capability of XRISM. The large field of view (FoV) of $38' \times 38'$ realized by Xtend encompasses the $3' \times 3'$ FoV of Resolve in its center. The finer pixel size of $1''.74$ of Xtend compared to that of $30''$ of Resolve well over-samples the point spread function of the XMA with an angular resolution of $1'.7$ and provides more detailed spatial information. On the other hand, Resolve realizes an unprecedented energy resolution of 7 eV in FWHM and will revolutionize our understanding of the X-ray Universe. Xtend and Resolve have their own characteristics in imaging and spectroscopy, respectively, and play complementary roles in XRISM.

Xtend's SXI employs a new type of P-channel back-illuminated type CCD with a thick depletion layer of 200 μm,[7–9] following the *Hitomi* CCD camera.[10] Japan's fifth X-ray astronomy mission, *Suzaku* carried

Further author information: (Send correspondence to K.M.)
K.M.: E-mail: mori@astro.miyazaki-u.ac.jp, Telephone: 81 985 58 7371

four CCD cameras, one of which used a back-illuminated type CCD with a depletion layer thickness of about 40 μm.[11] Fig. 2 shows X-ray spectra of G21.5−0.9 taken with the *Hitomi* and the *Suzaku* CCD cameras,[12,13] indicating the power of the thicker depletion layer of the CCD employed by the *Hitomi* X-ray CCD camera and also the Xtend's SXI. The thick depletion layer is effective also in the reduction of the non X-ray background (NXB) level above 6 keV.[14] Xtend's XMA and *Hitomi* X-ray mirror follow the concept of the *Suzaku* X-ray mirror,[15] nesting thin aluminum foils coated with gold with a pre-collimator for the reduction of the stray light. However, XMA's enlargement in the outer diameter from 40 cm to 45 cm with the longer focal length leads to the increase of the effective area by a factor of ∼1.5.[16] The high detection efficiency and low NXB level of the SXI and the large effective area of the XMA, in addition to the imagining capability described above, characterize the Xtend as a science instrument onboard XRISM.[3,6]

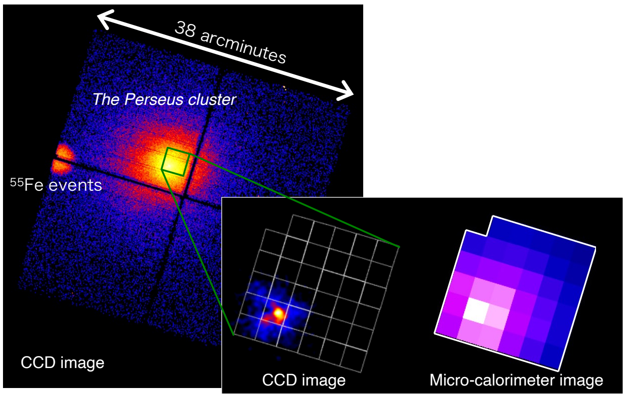


Figure 1. X-ray images of the Perseus Cluster (left) and its central radio galaxy NGC 1275 (right) taken with *Hitomi*.[14] The intensity scales of the two CCD images (left and right) are different to show the fainter entire cluster view and its bright central object. White grids superimposed on the CCD image of NGC 1275 indicate the micro-calorimeter pixel array.

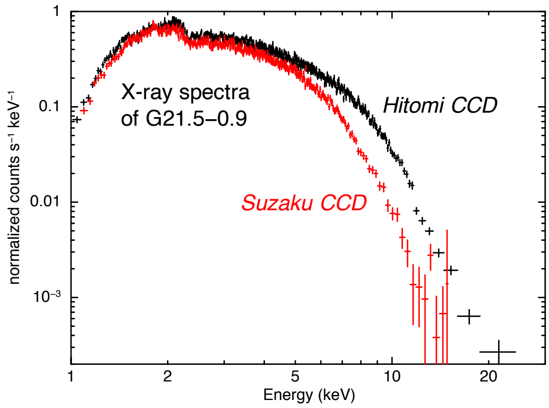


Figure 2. X-ray spectra of G21.5−0.9 taken with *Hitomi*[12] (black) and *Suzaku*[13] (red) CCD cameras. *Suzaku* carried four CCD cameras and the *Suzaku* spectrum was taken from the one using a back-illuminated type CCD.

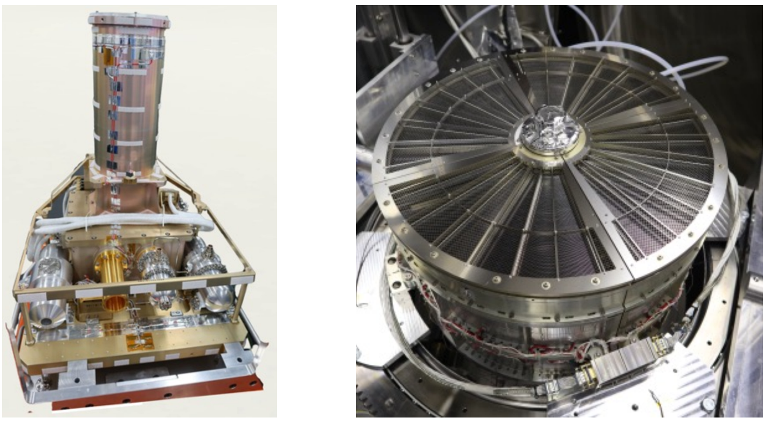


Figure 3. Photographs of the flight models of the SXI camera body (left) and XMA (right).

We have completed the fabrication of the flight models of both SXI and XMA as shown in Fig. 3. The performance verification has been successfully conducted in a series of sub-system level tests. We also carried out on-ground calibration measurements. In this paper, we report the current status of Xtend and describe the performances of the sub-system tests and calibration measurements, focusing on the SXI. The calibration studies of the XMA are presented elsewhere.[17–19] CCD spectra shown below are all made with grade 0, 2, 3, 4, and 6 events unless otherwise indicated. The confidence level of uncertainties attached is 68% throughout

this paper.

2. XTEND OVERVIEW

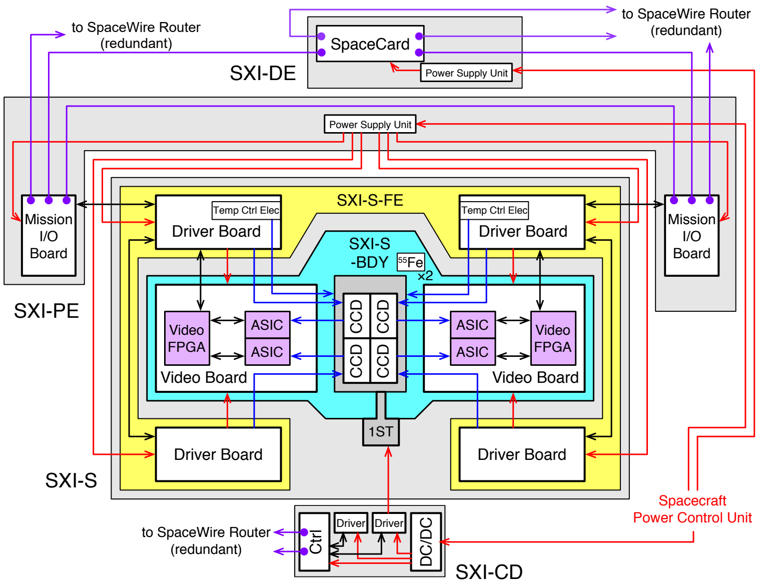


Figure 4. Block diagram of the SXI system. Red, blue, black, and purple lines indicate power supply, analog signal, digital signal, and SpaceWire connections, respectively.

The overall designs of the SXI and XMA are basically identical to those of the *Hitomi* X-ray CCD camera and X-ray mirror, respectively. Fig. 4 shows the block diagram of the SXI system. The SXI consists of four major components: SXI-S, SXI-PE, SXI-DE, and SXI-CD. The detailed descriptions of each component and the changes in the CCD camera system from *Hitomi* to XRISM are given in Ref.10 and 6, respectively. We here provide a short summary of the SXI system. SXI-S is a sensor part and consists of a camera body, front-end electronics, and a single-stage Stirling cooler (1ST in Fig. 4). Four CCDs, arranged in a 2×2 grid, are installed in the camera body with video boards. Although the SXI system is designed to be capable of cooling CCDs down to −120°C with the Stirling cooler, we plan to operate the SXI with a CCD temperature of −110°C at least in the first years after the launch. Two ^{55}Fe radioisotopes are also installed for calibration purpose. SXI-PE is the pixel processing electronics which processes the CCD signals from the video board and provide the timing signals of the CCD clocks to the driver board. Each of the two mission I/O boards equipped with FPGAs is responsible for a pair of two CCDs. SXI-DE is the digital electronics which further processes the CCD data based on the information processed by SXI-PE and compiles X-ray event data. SXI-DE also controls the entire SXI system except for the Stirling cooler, which is operated by the cooler driver, SXI-CD.

The CCDs were manufactured by Hamamatsu Photonics K.K. as in the case of *Hitomi*.[10] Tab. 1 summarizes the specifications of the XRISM CCD, Pch-NeXT4A. Please note that physical and logical values refer to those before and after on-chip 2×2 binning, respectively. Figures and plots in the following sections are all made in the unit of the logical value. One CCD has four readout nodes, two of which are used to simultaneously read out two halves of the imaging area. Therefore, two "segments" per CCD are taken in a frame cycle. Although most items shown in Tab. 1 are the same as those of the *Hitomi* CCD, Pch-NeXT4, we introduced two major changes on the CCD structure.[6] One is to add another aluminum layer on the top of the originally existing aluminum layer, resulting in a 100 nm + 100 nm thick aluminum coat, and to insert an extra aluminum layer under the electrode layer for the sake of the secure reduction of visible and infrared light leaks.[20] The other is to employ a notch structure, which is a narrow implant in the CCD channel confining a charge packet to a fraction of the pixel volume to reduce the charge transfer inefficiency (CTI).[21] We also changed the screening criteria of flight candidate CCDs before shipment from the manufacturer[22] and successfully excluded ones with the CTI anomaly observed in the *Hitomi* CCDs.[10]

Table 1. Specifications and nominal operation parameters of the SXI CCD

CCD Specification	Architecture	Frame transfer
	Imaging area size	30.720 mm × 30.720 mm
	Pixel format (physical/logical)	1280 × 1280 / 640 × 640
	Pixel size (physical/logical)	$24\mu m \times 24\mu m$ / $48\mu m \times 48\mu m$
	Depletion layer thickness	200 μm
	Incident surface layer (back side)	100 nm + 100 nm thick Aluminum coat
	Readout nodes (equipped/used)	4 / 2
Operation parameters	Frame cycle	4 seconds
	On-chip binning	2×2
	Charge injection	every 160 physical rows

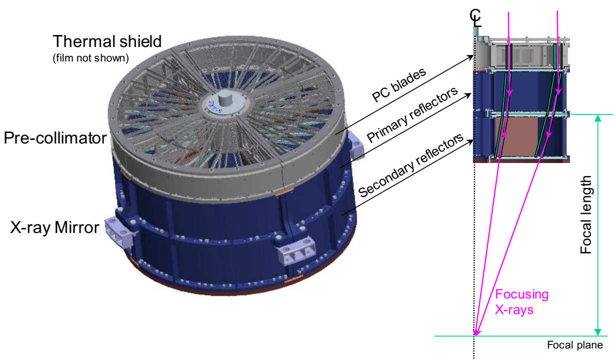


Figure 5. Schematic drawing of the XMA.

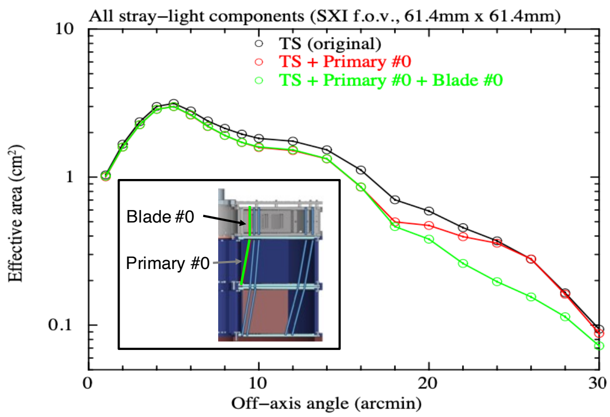


Figure 6. Effective area curves as a function of off-axis angle for the stray light component at 1 keV in three cases: no change from *Hitomi* (black), adding Primary #0 (red), and adding Primary #0 and Blade #0 (green). The inset shows where Primary #0 and Blade #0 are inserted.

Fig. 5 shows schematic drawings of the XMA. The XMA conically approximates Wolter-I grazing incidence optics. The effective diameter ranges from 116 to 450 mm. Each of the primary and secondary stages nests 203 reflectors. A reflector consists of an aluminum substrate with epoxy-replicated gold smooth surface for enhanced X-ray reflection. The thickness and height are 0.15–0.3 mm and 101.6 mm, respectively. The pre-collimator, placed in front of the primary stage for the reduction of the stray light, contains co-axially nested cylindrical aluminum blades arranged right above reflectors. A thermal shield is attached on the top of the pre-collimator to stabilize the thermal condition of the XMA. Although this design follows that of the *Hitomi* X-ray mirror, a change to reduce the amount of the stray light at large off-axis angles is introduced. Fig. 6 shows the idea of this change and its effect. In the *Hitomi* X-ray mirror design, the innermost reflector in the second stage is exposed to directly incoming X-rays, which could result in the stray light at large off-axis angles. Inserting an extra blade in the pre-collimator and an extra reflector in the primary stage, blade #0 and primary #0 in Fig. 6, eliminates the light path and effectively reduces the amount of the stray light. It also helps to reduce the possibility of the MMOD focusing.

3. SXI PERFORMANCE VERIFICATION IN SUB-SYSTEM TESTS

As of writing this paper, the SXI is installed into the spacecraft body and undergoes functional tests in a course of the spacecraft checkout. Before the installation, we successfully conducted a series of performance verification tests in sub-system level, including the thermal vacuum, vibration, and acoustic tests, as shown in Fig. 7. In the SXI thermal vacuum test held in October 2021, we verified X-ray imaging and spectroscopic performances in the full flight configuration for the first time. Since the SXI camera body is not vacuum-tight,

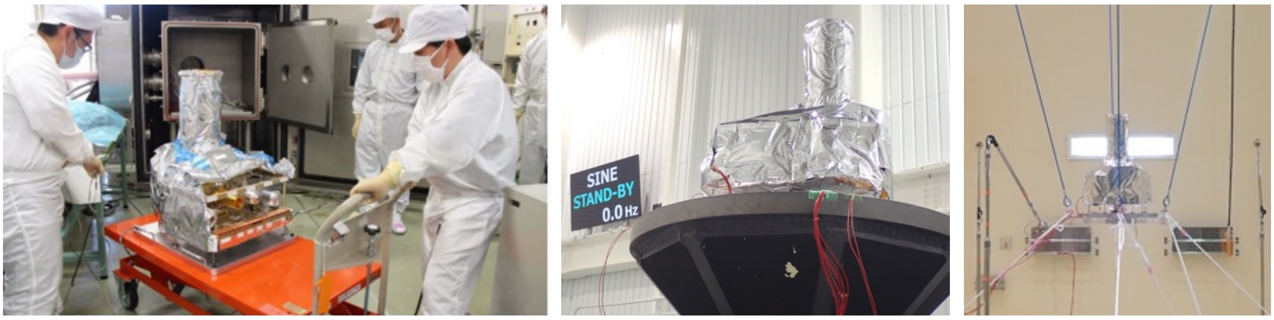


Figure 7. Photographs of the SXI thermal vacuum, vibration, and acoustic tests from left to right. These photographs are available at the XRISM social media sites.

the thermal vacuum test, in which the whole camera body is put into a large vacuum chamber as shown in Fig. 7 left, was the only occasion for us to verify its performance in the full flight configuration.

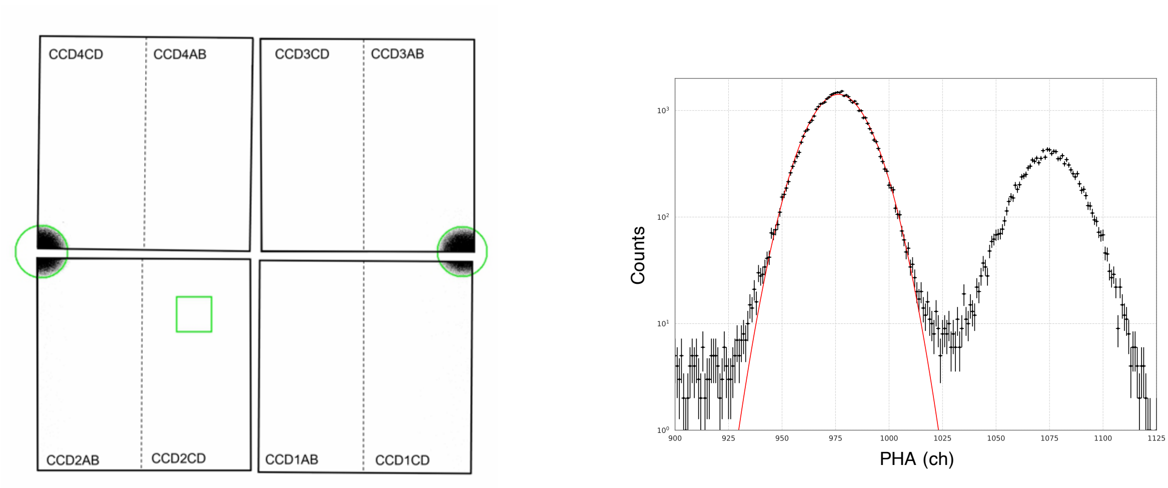


Figure 8. (left) Count map of X-ray events taken in the thermal vacuum test in a look-down view. Green circles encompass irradiated regions from the ^{55}Fe calibration sources. Black boxes and a green box indicate imaging areas of the four CCDs and that of the X-ray micro-calorimeter, respectively. Dashed lines correspond to boundaries of the CCD segments. Names of the CCDs (1–4) and segments (AB or CD) are superimposed. (right) Spectrum of X-ray events taken in the thermal vacuum test. The spectrum is made using the data taken in the segment CCD2AB. The red curve is the best-fit single Gaussian to the Mn-Kα line.

Fig. 8 shows a count map and spectrum of X-ray events from the ^{55}Fe calibration source taken in the thermal vacuum test. From the count map, we confirmed that the count rate, irradiated location, and region size are as designed. The spectrum is made with events taken in the segment CCD2AB, and CTI corrections[23,24] are not applied. The energy resolution of this spectrum is 177.5$\pm$0.6 eV in FWHM and as expected from on-ground calibrations held in advance, which is discussed in the next section.

Fig. 9 shows the time history of energy resolutions measured in the four segments irradiated with X-rays from the calibration sources as well as that of temperatures of the chamber, camera body, video, driver boards, and CCD. The spectrum in Fig. 8 is an integrated one during the entire time period shown in Fig. 9. In this thermal vacuum test, the temperature of the camera body was forced to swing from the hottest case (+17 °C) to the coldest case ($-$20 °C) defined by the system, during which the SXI system successfully kept the CCD temperature constant at $-$120 °C. The temperatures of the video and driver boards are not under control in the SXI system. It was verified that the energy resolutions of the CCDs are stable within the statistical uncertainties and insensitive to external thermal environment variations.

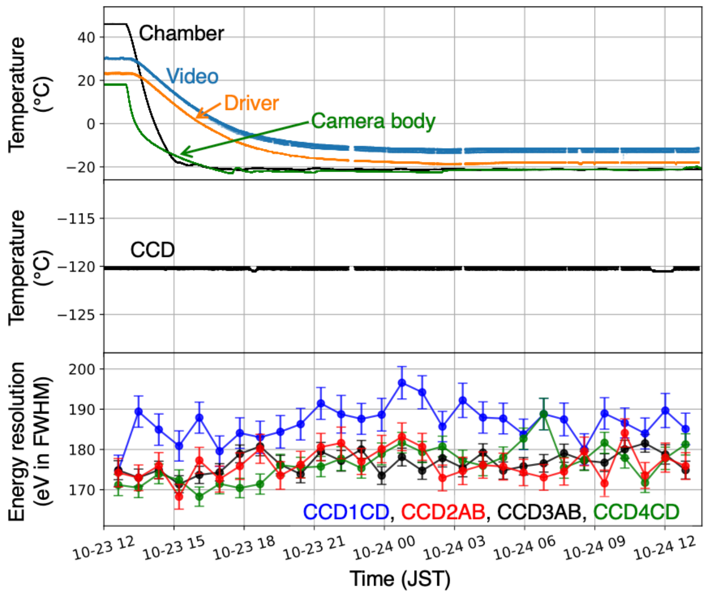


Figure 9. Time histories of temperatures of the chamber, video board, driver board, and camera body (top), CCD temperature (middle), and energy resolutions measured in the segments of CCD1CD, CCD2AB, CCD3AB, and CCD4CD (bottom).

4. SXI ON-GROUND CALIBRATION

We conducted the SXI on-ground calibration in two stages. In the first stage, the flight CCDs were installed in a camera system built in our laboratory and their spectroscopic performances were measured with multi-color X-ray data. The details of the system and the multi-color X-ray generator were described in Ref.22. Fig. 10 shows X-ray spectra taken in this system. The point in the first stage is that the noise environment and overall gain in this system are different from those in the flight configuration even if the degree of the differences would not be significant. Thus, the calibration purpose in this stage is to derive calibration parameters that are basically independent from the differences, and the main focus is to measure the energy dependence of the line center, energy resolution, CTI, and so on, as shown in Fig. 11. In the second stage, the calibration was performed in the full flight configuration except for replacement of the camera bonnet in order to make it vacuum-tight. An ^{55}Fe source was attached in the non-flight vacuum-tight bonnet and the entire areas of the four CCDs were irradiated with X-rays from the source. The point in the second stage is that the data is available only from the ^{55}Fe source, not from multi-color X-ray sources. Thus, the calibration purpose in this stage is to drive absolute calibration parameters at the energies of Manganese lines. Combining the results from the first and second stage measurements, we fully obtain the calibration parameters. The reason why we took this two-stage way in our calibration is two-fold. One is from a safety reason. We avoided unexpected risk that would have damaged flight electronics by using the multi-color X-ray generator, which requires high voltage, onto the flight camera body. The other is from a scheduling point of view. In this way, the flight camera fabrication can be proceeded in parallel to the first stage of the calibration, which was quite beneficial in the SXI development this time.

The on-ground calibration was performed with the CCD temperature of −110 °C, which is the initial operating temperature in orbit. On the other hand, the thermal vacuum test was performed with the CCD temperature of −120 °C in order to verify the cooling capability of the SXI system.

Fig. 12 shows pulse heights of grade 0 events in an energy band which includes Mn-Kα and Mn-Kβ lines as a function of row number, which is namely half of the number of transfer because of the on-chip binning, before and after the CTI correction. Spectra before and after the CTI corrections also shown. The data is taken in the second stage of the calibration. Parameters of the CTI correction are derived following Ref.24. Before the CTI correction, the pulse height generally decreases as a function of row number with periodic recovery at the

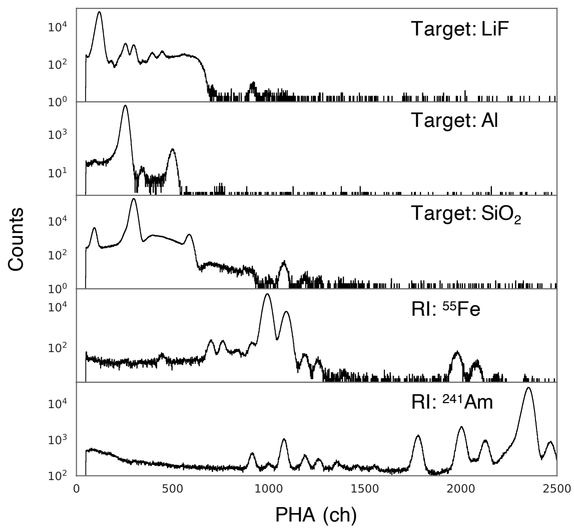


Figure 10. Spectra taken in the on-ground calibration using multi-color X-ray generator,[22] in which the secondary targets as well as radioisotopes can be changed without breaking vacuum. Top three and bottom two show spectra using the secondary targets and the radioisotopes in the figure, respectively. Background lines from the materials contained in this system and pile-up lines are also seen.

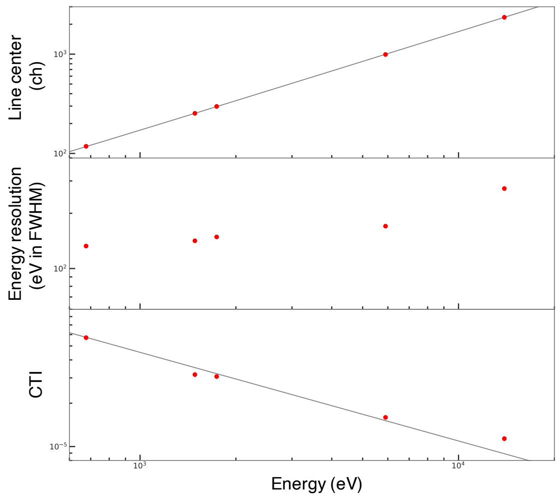


Figure 11. Energy dependence of line center (top), energy resolution (middle), and CTI (bottom). The values of the line center and energy resolution are derived from the single Gaussian fit to the spectra in Fig. 10. The CTI values in the bottom plot are specifically $c_{0\mathrm{F_I}}$ described in Ref.24. The best-fit linear function and power function are superimposed in the top and bottom plot, respectively.

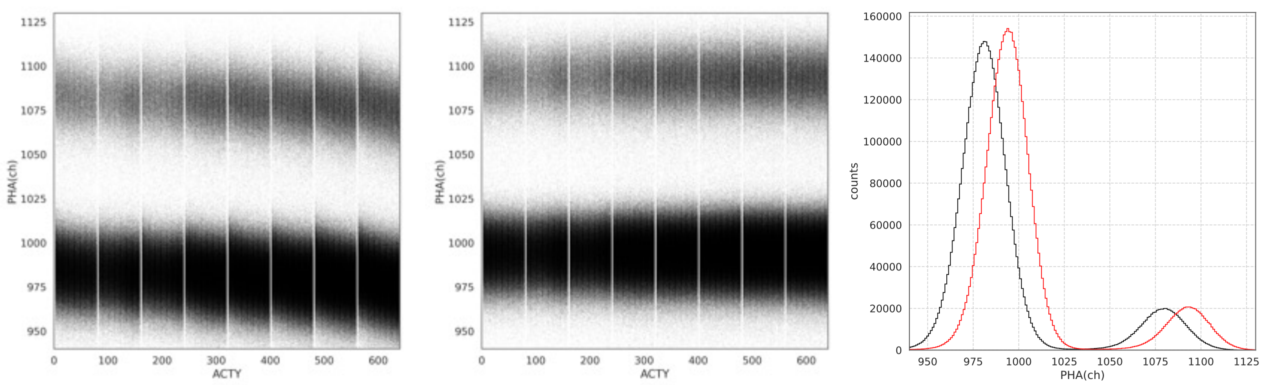


Figure 12. Pulse heights of grade 0 events in an energy band which includes Mn-Kα and Mn-Kβ lines as a function of row number before (left) and after (middle) the CTI correction. (right) Spectrum before (black) and after (red) the CTI correction.

charge injection (CI) rows, which are placed every 80 rows. This saw-tooth shape is the characteristics of the operation with the CI technique.[25] After the CTI correction, the saw-tooth shape disappears and the pulse height does not depend on the row number as is expected in the case without charge loss during transfer. It is also clear that the CTI correction makes the peak and width of the spectrum higher and narrower, respectively.

Tab. 2 summarizes the energy resolution of the CTI-corrected spectra extracted from various regions. Each Mn-Kα line is fitted with a single Gaussian and the FWHM derived in the unit of eV are written. The "cal. source region" and "on-axis region" are indicated by the green circles and the green box in Fig. 8 left,

Table 2. Summary of energy resolution measured with Mn-Kα lines in the unit of eV in FWHM

segment	entire region	cal. source region	on-axis region
CCD1AB	178.9±0.1		
CCD1CD	176.9±0.1	182.6±0.5	
CCD2AB	163.4±0.1	163.8±0.4	
CCD2CD	162.5±0.1		161.9±0.2
CCD3AB	166.0±0.1	168.1±0.3	
CCD3CD	168.4±0.1		
CCD4AB	164.5±0.1		
CCD4CD	168.9±0.1	173.2±0.4	

respectively. The spectrum taken from the "entire region of the segment CCD2CD" is actually shown in Fig. 12. At a given segment, the energy resolution of the cal. source region is always worse compared to that of the entire region because the cal. source region is located at the farthest point from the read-out nodes. The energy resolution of the cal. source region in CCD2AB shown here (163.8±0.4 eV) is better than that in the thermal vacuum test (177.5±0.6 eV) in spite of the higher temperature in the on-ground calibration. This is simply because the improvement due to the CTI correction is more than the degradation due to the higher temperature, especially for the data taken at the farthest point from the read-out nodes. We note that the energy resolution of the cal. source region in CCD2AB was 178.2±0.4 eV before the CTI correction. Among the values in Tab. 2, the best one is obtained at the on-axis region, which is as we intended when we determined the position of the CCDs. The mission requirement in the value of the energy resolution at the beginning of life is 200 eV or less. All the values in Tab. 2 are well below 200 eV with sufficient margin and we confirmed that our flight CCDs satisfy the mission requirement.

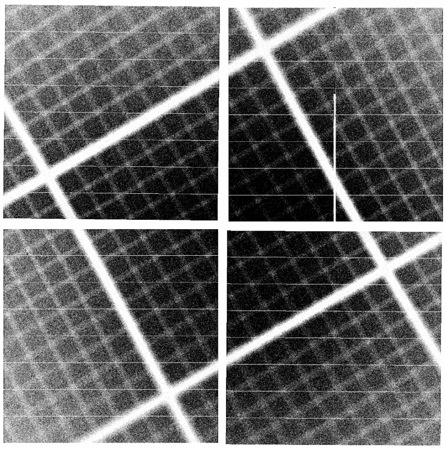


Figure 13. Count map of X-ray events taken in the second stage of the on-ground calibration in a look-down view. A non-flight mesh frame was placed just above the CCDs in this experiment.

Fig. 13 shows a count map of X-ray events taken in the second stage of the on-ground calibration. In this setup, a non-flight mesh frame was placed just above the CCD. The mesh was removed when the vacuum-tight bonnet was replaced with the flight bonnet before the installation of the SXI to the spacecraft body. We determined the relative orientation of the CCDs aligning the shadows of the mesh bars. Gaps between active pixel regions are then obtained to be $45''$–$60''$.

5. SUMMARY

We described the overview of Xtend, a soft X-ray imaging telescope onboard XRISM. We completed the fabrication of the flight model of both SXI and XMA. Regarding the SXI, a series of sub-system level performance verification tests was successfully conducted. On-ground calibration measurements were also performed and the spectroscopic performance of the SXI was confirmed to satisfy the mission requirement. Other calibration studies are ongoing. As of writing this paper, the SXI system is installed into the spacecraft body and the XMA awaits the installation.

ACKNOWLEDGMENTS

We are deeply saddened by the passing of our colleague and co-author, Kiyoshi Hayashida. He launched the Xtend team and guided us until here as a principal investigator. We will miss him as a colleague, as a friend, and above all, as a good human being.

We acknowledge extensive supports from Hamamatsu Photonics K.K., Mitsubishi Heavy Industries Ltd., and Sumitomo Heavy Industries Ltd. to develop CCD, SXI system, and cooler component, respectively. This work was supported by JSPS KAKENHI Grant Numbers JP21H01095, JP19K21884, JP20H01941, JP20H01947, JP21K03615, JP20KK0071, JP18H01256, JP21H04972, JP25287042, JP22H01269, JP20H00175, JP21H04493, JP20K14491, JP20J20685, JP21J00031, JP21K13963, JP21J10842, JP21K20372.

REFERENCES

[1] Tashiro, M. et al., "Concept of the X-ray Astronomy Recovery Mission," Proc. SPIE **10699**, 1069922 (July 2018).

[2] Tashiro, M. et al., "Status of x-ray imaging and spectroscopy mission (XRISM)," Proc. SPIE **11444**, 1144422 (Dec. 2020).

[3] Hayashida, K. et al., "Soft x-ray imaging telescope (Xtend) onboard X-ray Astronomy Recovery Mission (XARM)," Proc. SPIE **10699**, 1069923 (July 2018).

[4] Ishisaki, Y. et al., "Resolve Instrument on X-ray Astronomy Recovery Mission (XARM)," *Journal of Low Temperature Physics* **193**, 991–995 (Dec. 2018).

[5] Iizuka, R. et al., "Ground-based x-ray calibration of the Astro-H/Hitomi soft x-ray telescopes," *Journal of Astronomical Telescopes, Instruments, and Systems* **4**, 011213 (Jan. 2018).

[6] Nakajima, H. et al., "Soft x-ray imager (SXI) for Xtend onboard X-Ray Imaging and Spectroscopy Mission (XRISM)," Proc. SPIE **11444**, 1144423 (Dec. 2020).

[7] Ozawa, H. et al., "Development of p-type CCD for the NeXT: the next Japanese x-ray astronomical satellite mission," Proc. SPIE **6266**, 62662N (June 2006).

[8] Takagi, S. et al., "Development of fully depleted and back-illuminated charge-coupled devices for soft x-ray imager onboard the NeXT satellite," Proc. SPIE **6266**, 62663V (June 2006).

[9] Ueda, S. et al., "Development of the x-ray CCD for SXI on board ASTRO-H," Proc. SPIE **8145**, 814504 (Sept. 2011).

[10] Tanaka, T. et al., "Soft X-ray Imager aboard Hitomi (ASTRO-H)," *Journal of Astronomical Telescopes, Instruments, and Systems* **4**, 011211 (Jan. 2018).

[11] Koyama, K. et al., "X-Ray Imaging Spectrometer (XIS) on Board Suzaku," PASJ **59**, 23–33 (Jan. 2007).

[12] Hitomi Collaboration, "Hitomi X-ray observation of the pulsar wind nebula G21.5-0.9," PASJ **70**, 38 (June 2018).

[13] Tsujimoto, M. et al., "Cross-calibration of the X-ray instruments onboard the Chandra, INTEGRAL, RXTE, Suzaku, Swift, and XMM-Newton observatories using G21.5-0.9," A&A **525**, A25 (Jan. 2011).

[14] Nakajima, H. et al., "In-orbit performance of the soft X-ray imaging system aboard Hitomi (ASTRO-H)," PASJ **70**, 21 (Mar. 2018).

[15] Serlemitsos, P. J. et al., "The X-Ray Telescope onboard Suzaku," PASJ **59**, 9–21 (Jan. 2007).

[16] Iizuka, R. et al., "Ground-based x-ray calibration of the Astro-H soft x-ray telescopes," in [*Space Telescopes and Instrumentation 2014: Ultraviolet to Gamma Ray*], Proc. SPIE **9144**, 914458 (July 2014).

[17] Boissay-Malaquin, R. et al., "Ground Calibration of the X-ray Mirror Assembly for the X-Ray Imaging and Spectroscopy Mission (XRISM) I - Measurement Setup and Effective Area," Proc. SPIE, in press (2022).

[18] Tamura, K. et al., "Ground calibration of the X-ray Mirror Assembly for the X-Ray Imaging and Spectroscopy Mission (XRISM) II - Imaging performance and stray light," Proc. SPIE, in press (2022).

[19] Hayashi, T. et al., "Ground Calibration of the X-ray Mirror Assembly for the X-Ray Imaging and Spectroscopy Mission (XRISM) III - Performance variation across the aperture," Proc. SPIE, in press (2022).

[20] Uchida, H. et al., "Optical blocking performance of ccds developed for the x-ray astronomy satellite xrism," *Nuclear Instruments and Methods in Physics Research A* **978**, 164374 (2020).

[21] Kanemaru, Y. et al., "Radiation hardness of a p-channel notch CCD developed for the X-ray CCD camera onboard the XRISM satellite," *Journal of Instrumentation* **14**, C04003 (Apr. 2019).

[22] Yoneyama, T. et al., "Screening and selection of xrism/xtend flight model ccd," *Nuclear Instruments and Methods in Physics Research A* **985**, 164676 (2021).

[23] Nobukawa, K. K. et al., "Use of a charge-injection technique to improve performance of the Soft X-ray Imager aboard ASTRO-H," *Nuclear Instruments and Methods in Physics Research A* **765**, 269–274 (Nov. 2014).

[24] Kanemaru, Y. et al., "Experimental studies on the charge transfer inefficiency of ccd developed for the soft x-ray imaging telescope xtend aboard the xrism satellite," *Nuclear Instruments and Methods in Physics Research A* **984**, 164646 (2020).

[25] Uchiyama, H. et al., "New CTI Correction Method for Spaced-Row Charge Injection of the Suzaku X-Ray Imaging Spectrometer," PASJ **61**, S9–S15 (Jan. 2009).